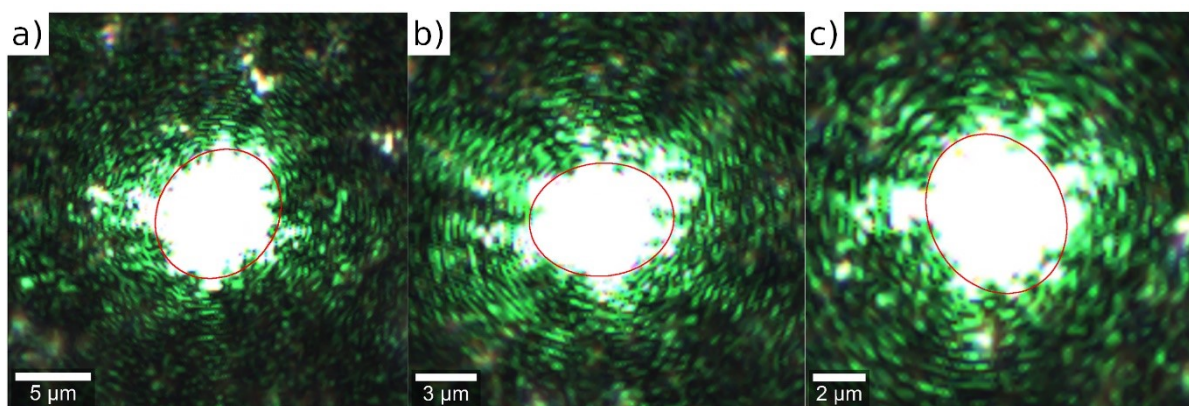**Supplementary Info**

Estimation of laser spot size

Figure S1: Microscope images of the laser spot. The areas of the red ellipses were determined in Fiji utilising the scale bar as reference. (a): 55.239 μm²; (b): 30.879 μm²; (c): 25.272 μm²; Average: 37.13 ± 13.01 μm².

Determination of weighted peak positions in the WITec Project software[2]

The background of the spectra is determined as described in equation S1 and Fig. S2:

$$S_i = \tilde{S}_i - B(x_i)$$ (S1)

S_i: Spectrum without background
$\tilde{S}_i$: Spectrum with background
$B(x_i)$: Background estimation at position x_i
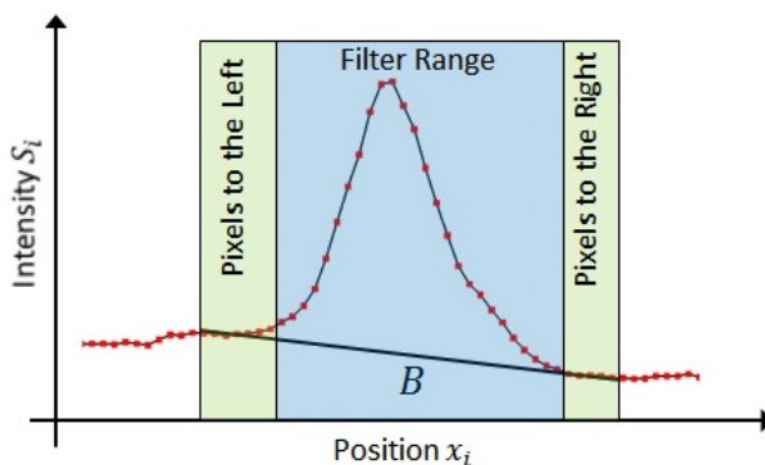x_i: Spectral position at pixel i

Figure S2: Schematic of determination of the spectral background of a distinct peak.[2]

Filter range is set by entering values for the centre of the range and a width. For background determination a number of pixels to the left and right of this range is set. The average of position and intensity determines the slope of the background.

The weighted position is then calculated as described in equation S2 and S3:

$$F_{sum} = \sum_{i=n_l}^{n_r} S_r \qquad (S2)$$

$$F_{CoM} = \frac{1}{F_{sum}} \sum_{i=n_l}^{n_r} x_i S_r \qquad (S3)$$

F_{sum}: Sum of intensities in the set range

n_l: Leftmost pixel of set range

n_r: Rightmost pixel of set range

F_{CoM}: Center of mass in the set range / weighted position of the signal

For all determined weighted peak positions of the IrO_2 E_g band in this work, 4 pixels to the left and right were set for background determination and the range was set to have a width of 80 cm^{-1} and to be centred around 545 cm^{-1}.

SEM Analysis of Ir powders

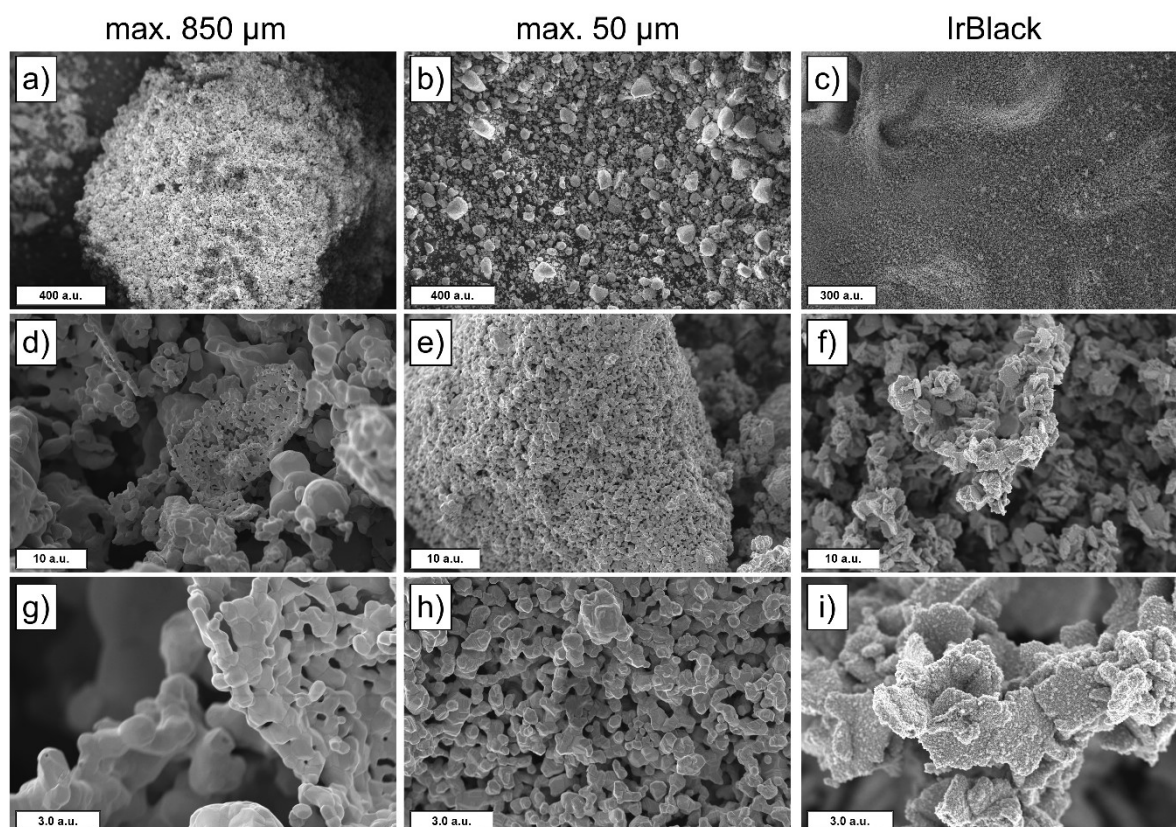max. 850 µm   max. 50 µm   IrBlack

Figure S3: SEM images of the three Ir powders in different magnifications. a): max. 850 µm Ir powder at 162x magnification, b): max. 50 µm Ir powder at 154x magnification, c): Ir Black at 162x magnification. d-f): max. 850 µm Ir powder/max. 50 µm Ir powder/IrBlack at 5000x magnification. g-h): max. 850 µm Ir powder/max. 50 µm Ir powder/IrBlack at 20000x magnification.

Test for surface enhancement of Raman signal

Surface enhancement of Raman signal due to plasmonic effects of the metallic iridium structures could influence signal strength of the IrO_2 bands. To test if the analyzed iridium particles exhibit any surface enhanced Raman spectroscopy (SERS) effect, methylene blue was utilized as analyte for Raman measurements. Methylene blue hydrate was sourced from Sigma-Aldrich in ≥97.0 % purity. Small amounts of the respective Ir powder were mixed with a 5 µl drop of 10^{-4} M aqueous solution of methylene blue. The mixtures were dried on a microscope glass slide in air and Raman measurements were performed with a 532 nm Laser with 0.2 mW, an acquisition time of 10 s and a Zeiss EC Epiplan-Neofluar HD Dic 10x / 0.25 objective. For reference the dried methylene blue solution was also measured once on its own.
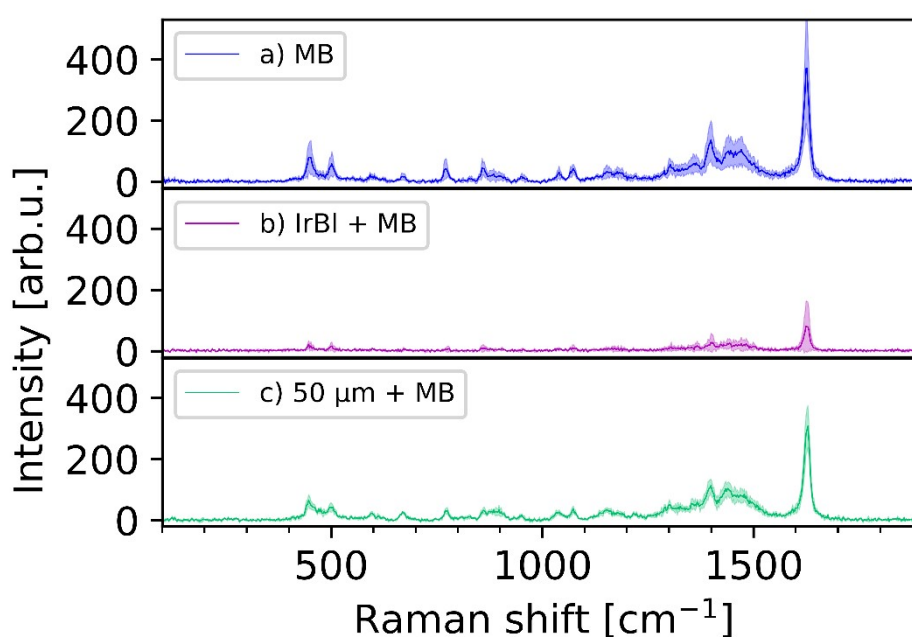

Figure S4: Average of three Raman measurements of a) Methylene blue, b) Methylene blue on IrBlack powder, c) Methylene blue on 50 µm powder. Standard deviations are displayed as colored areas around the curves.

The resulting spectra are depicted in Figure S4. No surface enhancement effect is observable, as the signal intensity of the methylene blue signals are generally weaker for the Ir powder mixtures than for the pure methylene blue sample. Therefore, an influence on IrO_2 signal intensity by plasmonic effects can be excluded. Thus, the signal intensities of iridium oxide species are only affected by the amount of IrO_2 formed by laser induced oxidation.
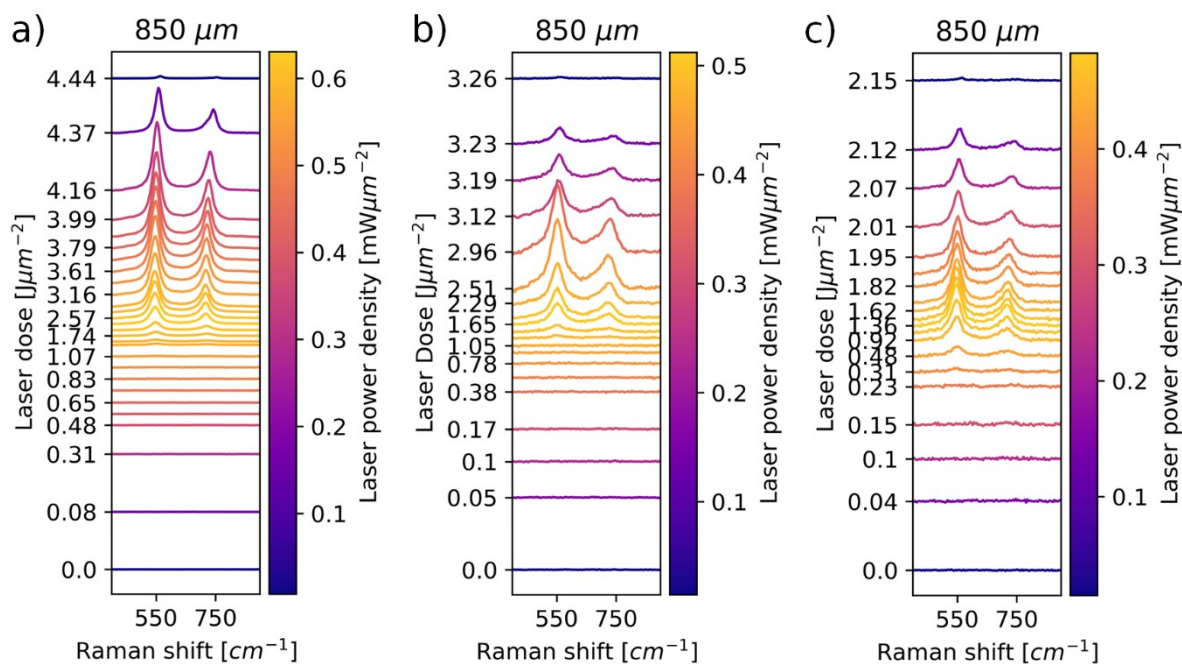
Laser power Series on iridium powders

Figure S5: Laser power series of iridium powder with particle size of 850 μm. Bands of crystalline IrO_2 (E_g @ 550 cm^{-1}, A_{1g} + B_{2g} @ 720 cm^{-1}) are observable at high laser powers, indicating an oxidation of the iridium metal.
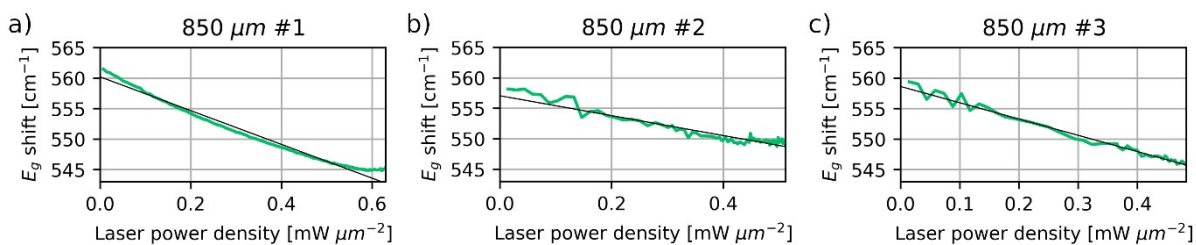

Figure S6: Weighted position of the E_g band and linear fit at decreasing laser power during the laser power series performed on 850 μm iridium powder.
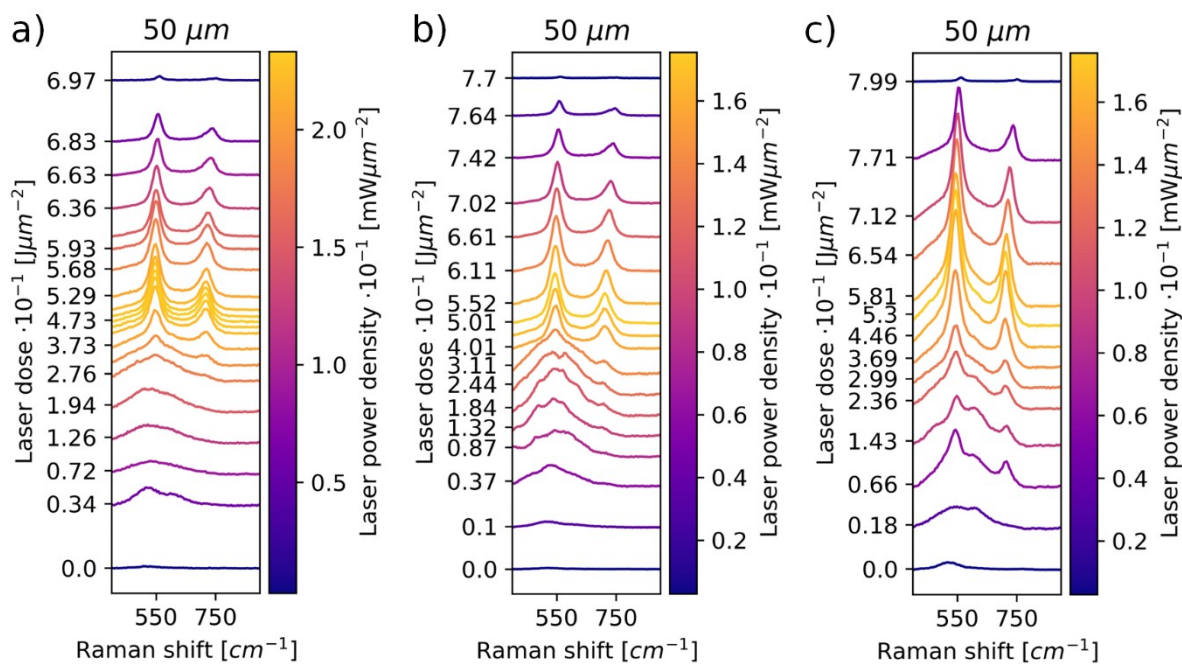
Figure S7: Laser power series of iridium powder with particle size of 50 μm. Bands of crystalline IrO_2 (E_g @ 550 cm^{-1}, A_{1g} + B_{2g} @ 720 cm^{-1}) are observable at high laser powers, indicating an oxidation of the iridium metal.
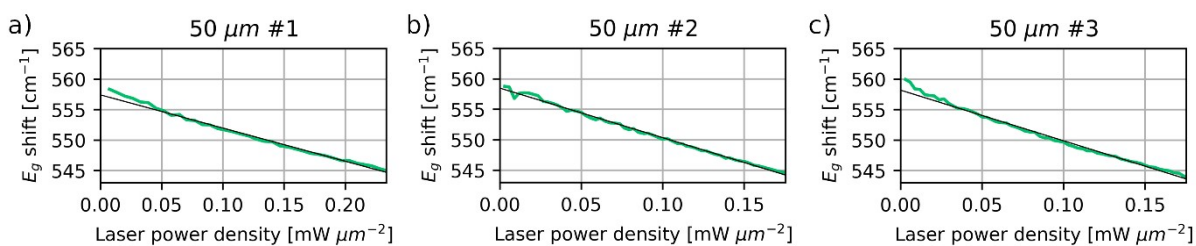

Figure S8: Weighted position of the E_g band and linear fit at decreasing laser power during the laser power series performed on 50 μm iridium powder.
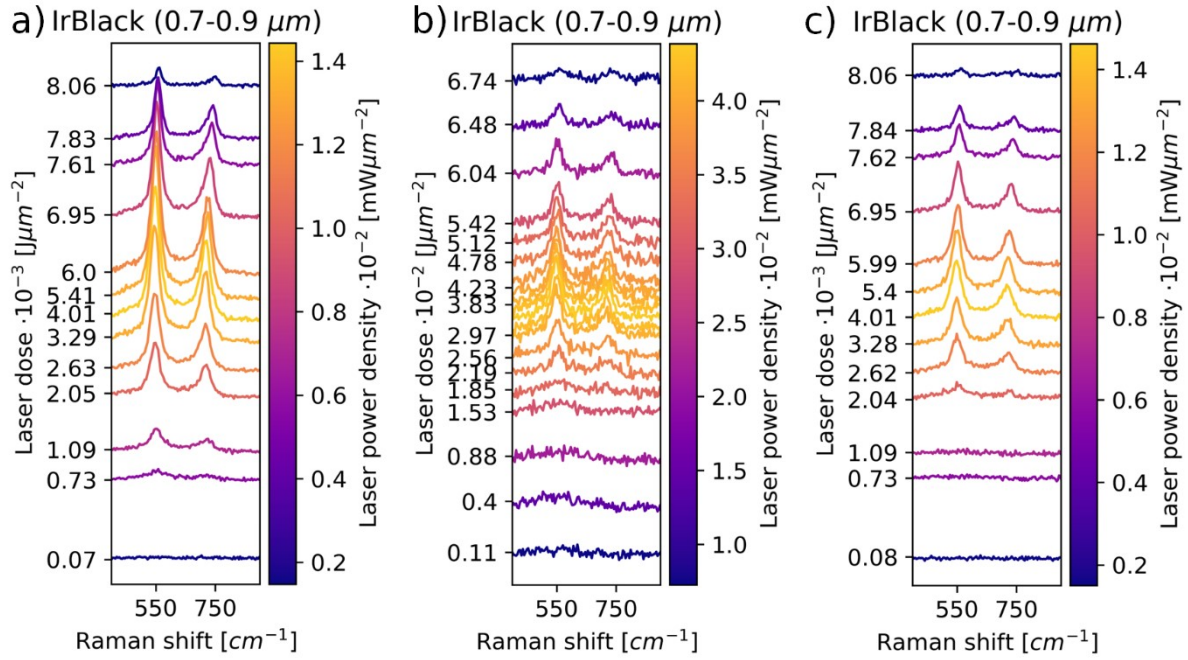
Figure S9: Laser power series of iridium black powder with particle size of 0.7-0.9 µm. Bands of crystalline IrO_2 (E_g @ 550 cm^{-1}, A_{1g} + B_{2g} @ 720 cm^{-1}) are observable at high laser powers, indicating an oxidation of the iridium metal.
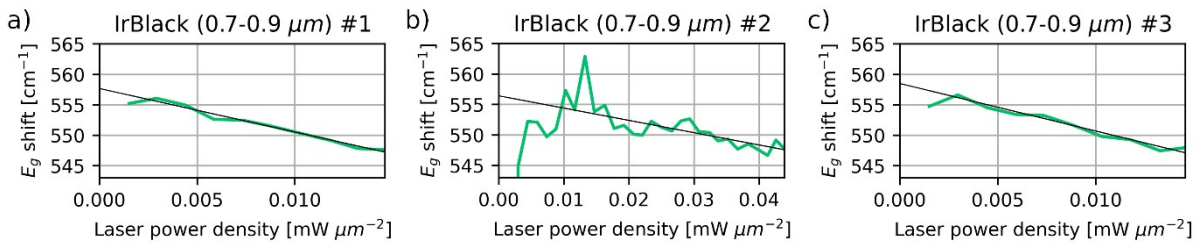

Figure S10: Weighted position of the E_g band and linear fit at decreasing laser power during the laser power series performed on 0.7-0.9 µm iridium black powder. Strong deviations from the trend, especially at the lower laser powers, are caused by low signal to noise ratio in the spectra.

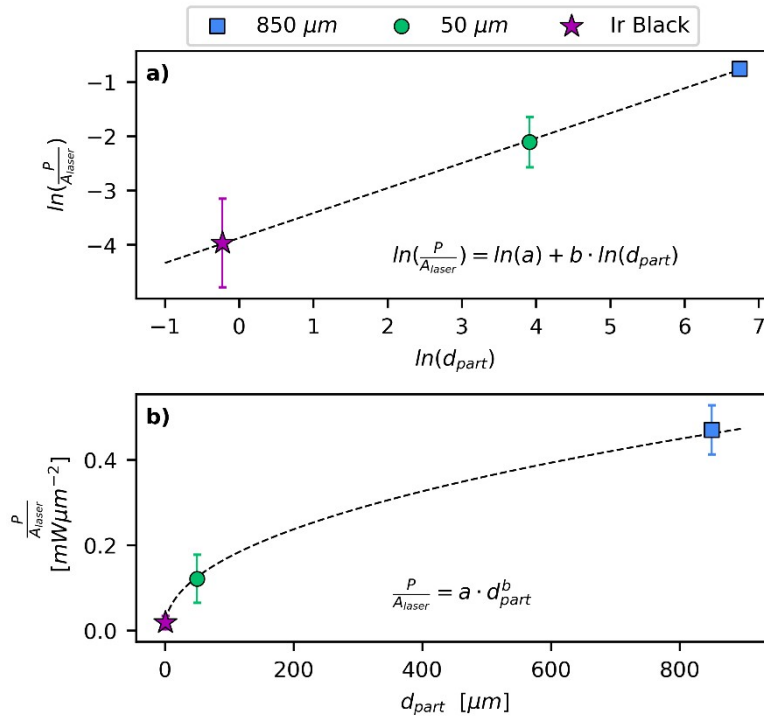**Dependence of laser power density on particle size**

Figure S11: Plots of Laser power density against the particle size with logarithmic (a) and linear scale (b). The parameters determined from the linear regression have the values a = -3.88±0.23 and b = 0.46±0.20.

Plotting the power density against particle size with logarithmic x and y axis scales yields a linear plot (Fig. S11 (a)). A polynomial relationship between laser power density and particle size can be derived using linear regression, which is shown in equations S4-S6.

$$\ln\left(\frac{P}{A_{laser}}\right) = \ln(a) + b \cdot ln(d_{part}) \tag{S4}$$

$$exp\left(\ln\left(\frac{P}{A_{laser}}\right)\right) = exp\left(\ln(a) + b \cdot ln(d_{part})\right) \tag{S5}$$

$$\frac{P}{A_{laser}} = a \cdot d_{part}^{\,b} \tag{S6}$$

P: Laser power
A_{laser}: Laser spotsize
a, b: Constants
d_{part}: Particle diameter

The computed expression for the dependence on particle diameter has its zero crossing at a particle diameter of 0.0 μm. Therefore, it shows a valid result for this edge case. While the overall polynomial dependence of the laser power density on particle size is therefore plausible, the physical origin for the factor a and the exponent b (Equations S4-6) is challenging to assess. Furthermore, the differences in morphology of the analyzed powders may add to the error of the method. While the data very accurately matches the computed formulas, more extensive analyses of controlled particle sizes and an increased statistical sample size should be employed for a more reliable assessment. Then, the computed expressions could possibly be utilized for an accurate determination of the particle size from the laser power density at oxidation onset for a given Raman setup.

Water electrolysis

The sample was operated in a zero-gap single cell PEM electrolyser under galvanostatic mode. The structure of the cell is shown in the supplementary information (Fig. S12). The Gas diffusion layer (GDL) of the anode side consists of platinum coated titanium fibre and sourced from NV Bekaert SA (Zwevegem, Belgium). For cell conditioning, the electrolyzer was operated at 1 A·cm^{-2} for two days at 60 °C. Feed water was supplied to both sides of the cell with 10 ml·min^{-1}. Afterwards, the current density was increased to 2 A·cm^{-2} and the flow rate was varied (Fig. S13). Each flow rate was kept constant for 12 h and polarization curves were measured at regular intervals. The high flow rates during the electrolysis were employed in order to expose the MEA to a deliberate accelerated stress test.
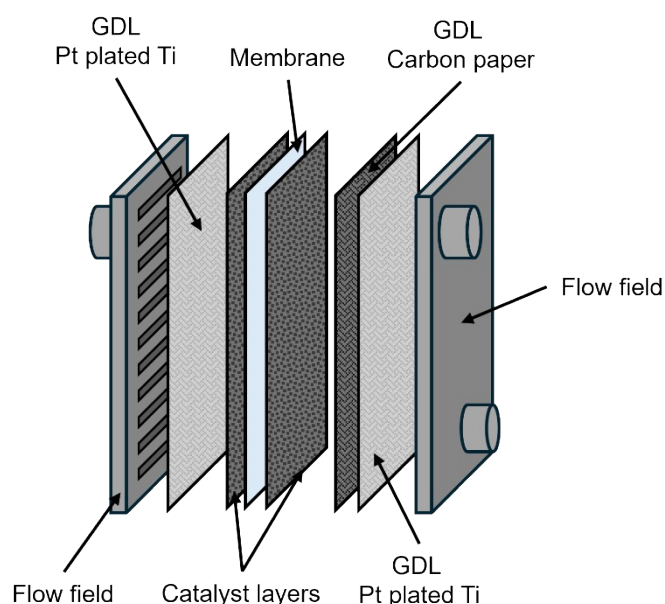

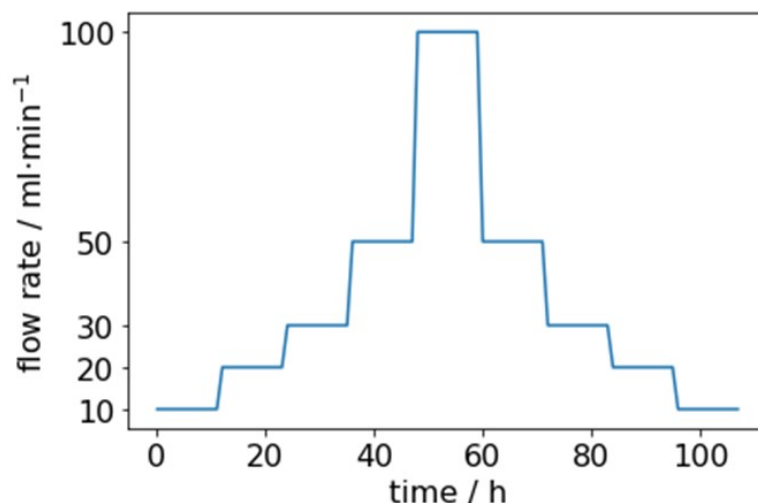Figure S12: Schematic of the cell construction utilised in the electrolysis operation.

Figure S13: Water flow rate variation during electrolyser operation.

Polarisation curves that were recorded at the start and end of the electrolyzer operation are depicted in Fig. S14. The curve at the start of the operation exhibits lower potentials than the curve that was recorded after the operation. A slightly increased overpotential can hint to a performance loss of the cell, which may be caused by changes in the physical properties of the MEA.
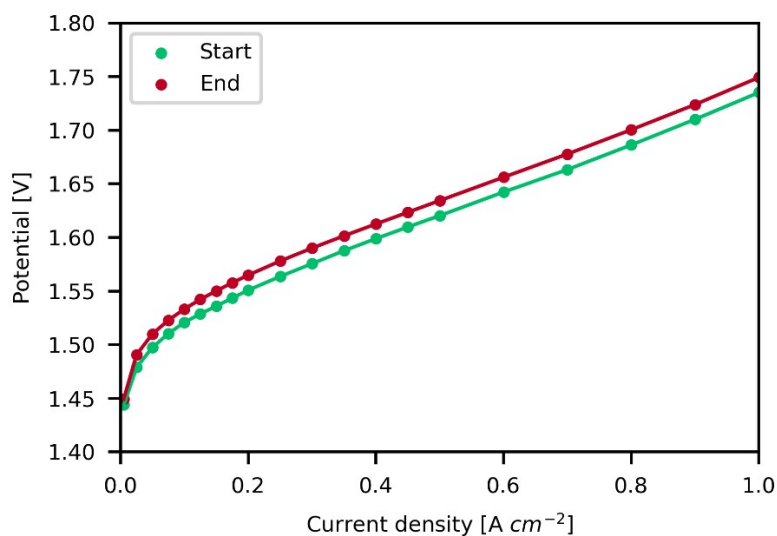

Figure S14: Polarization curves at the start (green) and end (red) of the one-week electrolyser operation. The polarization curves were recorded with a flow rate of 10 ml min^{-1}. A higher overpotential is observable at the end of operation, which indicates a small performance loss of the cell components.

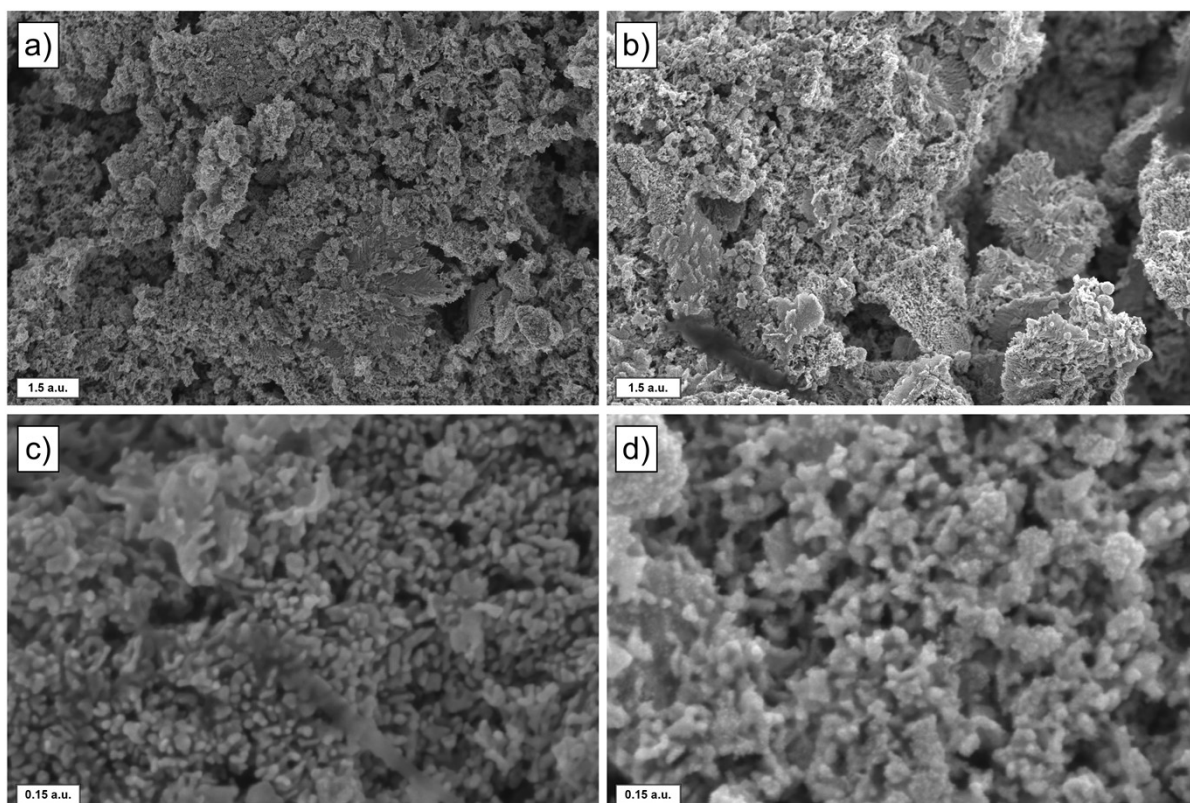**SEM images of pristine and operated MEA anodes**

Figure S15: SEM images of the MEA anode samples. Pristine (a) and operated sample (b) at 20000x magnification. Pristine (c) and operated (d) sample at 200000x magnification.

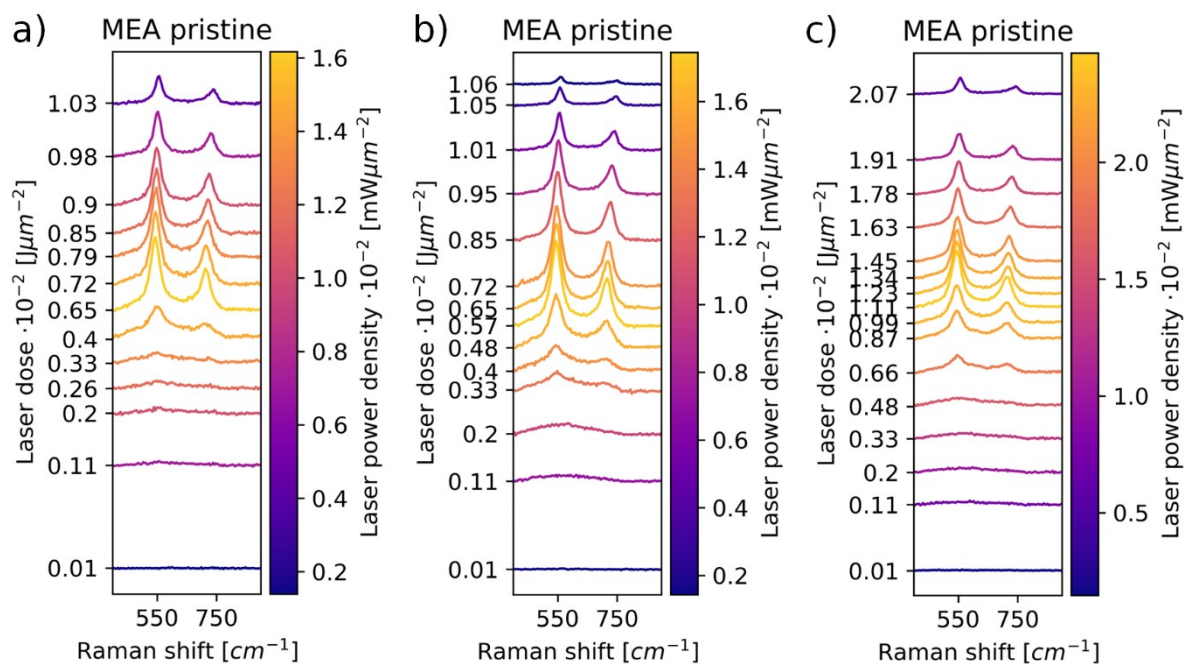**Laser power series on pristine and post operation MEA anodes**

Figure S16: Laser power series of the pristine MEA anode. Bands of crystalline IrO_2 (E_g @ 550 cm^{-1}, A_{1g} + B_{2g} @ 720 cm^{-1}) are observable at high laser powers, indicating an oxidation of the iridium metal.
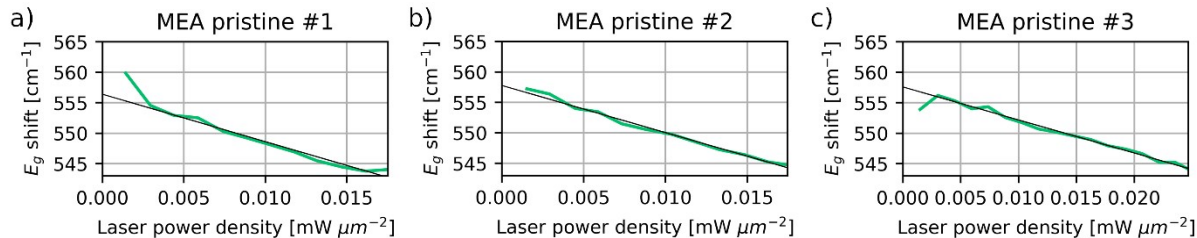

Figure S17: Weighted position of the E_g band and linear fit at decreasing laser power during the laser power series performed on the anode of the pristine MEA sample.
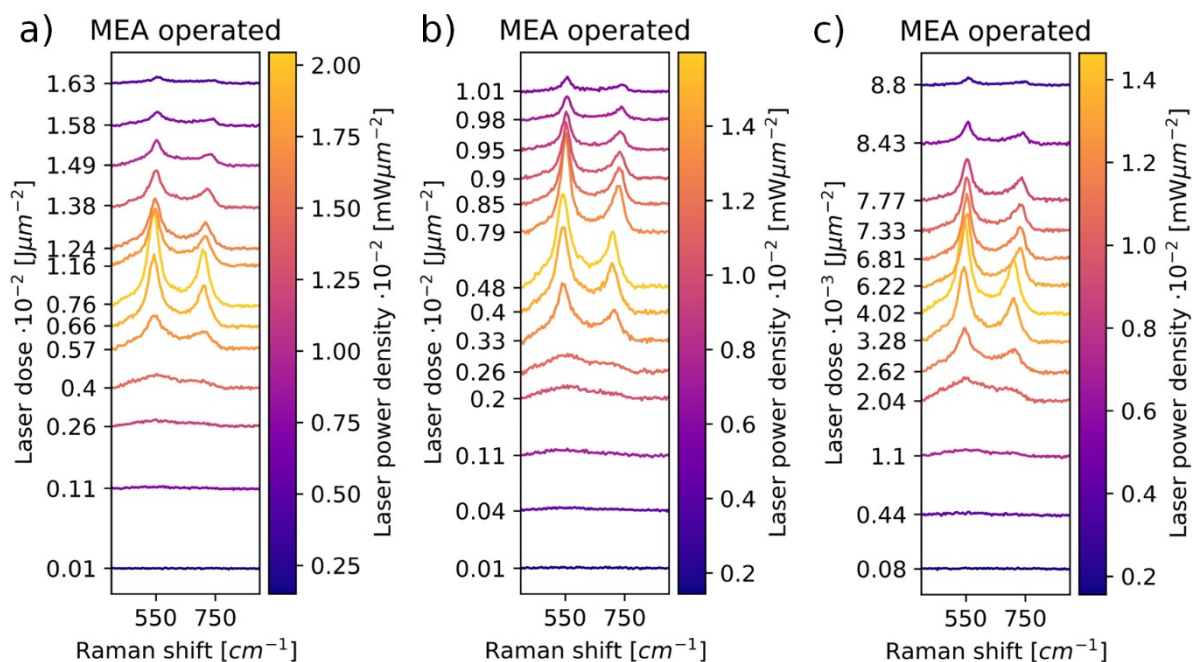
Figure S18: Laser power series of the pristine MEA anode. Bands of crystalline IrO_2 (E_g @ 550 cm^{-1}, A_{1g} + B_{2g} @ 720 cm^{-1}) are observable at high laser powers, indicating an oxidation of the iridium metal.
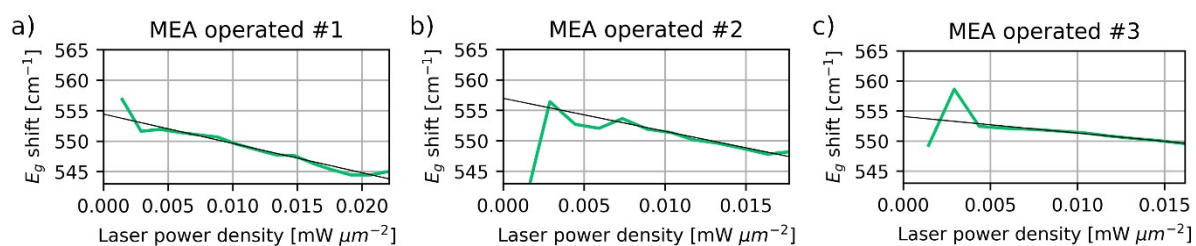

Figure S19: Weighted position of the E_g band and linear fit at decreasing laser power during the laser power series performed on the anode of the operated MEA sample. Strong deviations from the trend, especially at the lower laser powers, are caused by low signal to noise ratio in the spectra.
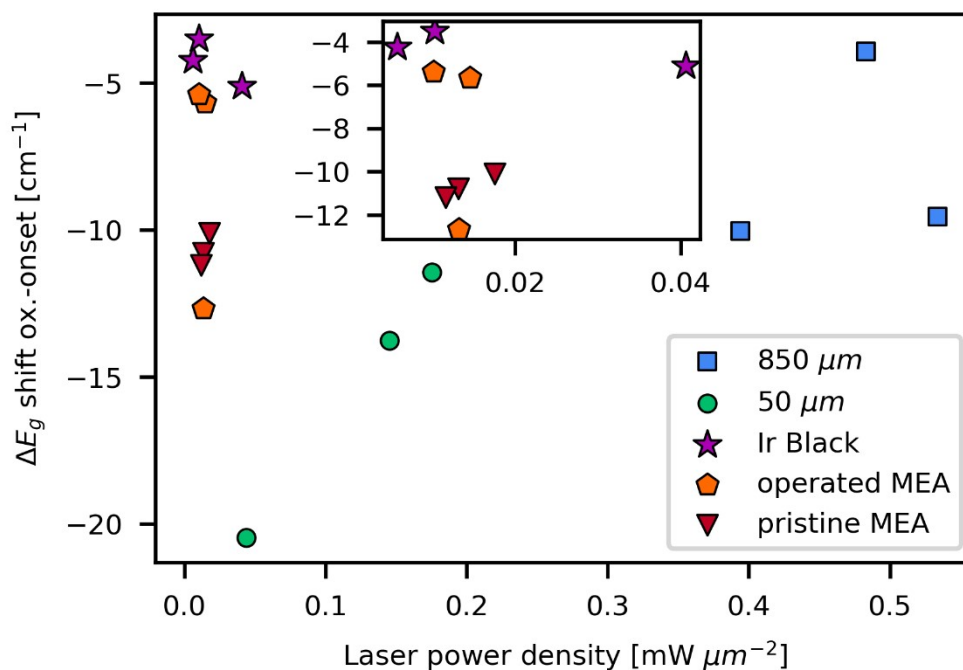
Figure S20: E_g band shift relative to the E_g shift at 0.0 mWμm^{-2} vs. Laser power densities on oxidation onset with respective standard deviations for all examined samples. Spectra in which the first IrO_2 signal was observable were selected and E_g band shift was obtained from deconvolution of the spectra. Deconvolution was used due to the weakness of the E_g band and overlapping with other signals for most of the measurements at oxidation onset. The E_g shift at 0.0 mWμm^{-2} was determined by interpolation from the data in Fig. S6, S8, S10, S17, S19.

References

1. Schindelin, J.; Arganda-Carreras, I.; Frise, E.; Kaynig, V.; Longair, M.; Pietzsch, T.; Preibisch, S.; Rueden, C.; Saalfeld, S.; Schmid, B.; Tinevez, J.-Y.; White, D. J.; Hartenstein, V.; Eliceiri, K.; Tomancak, P.; Cardona, A., *Nature Methods* **2012**, 9 (7), 676-682.

2. WITec Project, ver. 6.1.6.130, WITec, Ulm, Germany